This is a repository copy of *A new analysis procedure for detecting periodicities within complex solar coronal arcades*.

A New Analysis Procedure for Detecting Periodicities within Complex Solar Coronal Arcades

Farhad Allian[1] , Rekha Jain[1] , and B. W. Hindman[2]
[1] School of Mathematics and Statistics, University of Sheffield, Sheffield S3 7RH, UK; fallian1@sheffield.ac.uk
[2] JILA, NIST and University of Colorado, Boulder, CO 80309-0440, USA

Abstract

We study intensity variations, as measured by the Atmospheric Imaging Assembly on board the *Solar Dynamics Observatory*, in a solar coronal arcade using a newly developed analysis procedure that employs spatio-temporal autocorrelations. We test our new procedure by studying large-amplitude oscillations excited by nearby flaring activity within a complex arcade and detect a dominant periodicity of 12.31 minutes. We compute this period in two ways: from the traditional time–distance fitting method and using our new autocorrelation procedure. The two analyses yield consistent results. The autocorrelation procedure is then implemented on time series for which the traditional method would fail due to the complexity of overlapping loops and a poor contrast between the loops and the background. Using this new procedure, we discover the presence of small-amplitude oscillations within the same arcade with 9.13 and 9.81 minute periods prior and subsequent to the large-amplitude oscillations, respectively. Consequently, we identify these as "decayless" oscillations that have only been previously observed in nonflaring loop systems.

Key words: Sun: activity – Sun: atmosphere – Sun: corona – Sun: flares – Sun: oscillations

1. Introduction

Solar coronal arcades consist of brightly illuminated arches of hot plasma referred to as coronal loops. The arcades can act as waveguides for magnetohydrodynamic (MHD) waves, and these waves are of particular interest due to their diagnostic value in estimating the magnetic properties of arcades through seismology. Theoretical studies by Edwin & Roberts (1983) and Roberts et al. (1984) have, so far, formed the basis for most models of wave propagation in solar coronal loops. These studies describe the propagation of magnetohydrodynamic (MHD) waves along straight magnetic tubes. In particular, many previous seismic analyses have attributed the observed oscillations to the motions of fast kink waves. Theoretical studies of the wave propagation in arcades with curved field lines, or loops, have been rarer. Smith et al. (1997), Brady & Arber (2005), and Selwa et al. (2007) have numerically studied fast MHD waves in dense curved potential field loops. Smith et al. (1997) focused on the leakage of such waves across field lines with an exponentially increasing Alfvén speed profile. Brady & Arber (2005) studied a similar model, but with an inverse linear Alfvén speed profile, and concluded that the oscillation damping rate is proportional to the period. Selwa et al. (2007) considered a similar curved-arcade loop model and demonstrated that the main source of the wave attenuation was through such leakage. Moreover, Verwichte et al. (2006a) and Verwichte et al. (2006b) studied analytically the effects of vertically polarized fast MHD waves in a curved coronal loop with a linear Alfvén speed profile. Recently, Hindman & Jain (2015, 2018) have demonstrated that fast MHD waves can be fully trapped by the magnetic field in an arcade under fairly common circumstances. Thus, fast waves can form resonances and wave leakage is not necessarily an essential process.

Since the advent of the *Transition Region and Coronal Explorer* (*TRACE*), wave propagation in coronal loops has been observed in the extreme ultraviolet (EUV) as the loops oscillate in response to the passage of transient MHD waves from nearby flares (Aschwanden et al. 1999; Nakariakov et al. 1999; Li et al. 2017). Such loops exhibit transverse standing oscillations with periods ranging from a few minutes to several tens of minutes. Aschwanden et al. (2002) investigated 17 events with *TRACE* data and concluded that most of the oscillating loops do not fit the simple model of kink eigenmode oscillations, but instead suggest that the oscillations are flare-induced impulsively generated MHD waves, which decay rapidly either due to damping or wave leakage. Such observed large-amplitude attenuation has been generally attributed to resonant absorption, a mode conversion process whereby energy is transferred from the global transverse waves to local Alfvénic waves (e.g., Goossens et al. 2002; Ruderman & Roberts 2002; Hindman & Jain 2018). An alternate theory has also been proposed that explains the rapid signal attenuation as an interference effect that occurs whenever wave packets propagate along a multidimensional waveguide Hindman & Jain (2014).

With high-cadence data from the Atmospheric Imaging Assembly (AIA) on board the *Solar Dynamics Observatory* (*SDO*; see Lemen et al. 2012), it is now clear that multiple loops within a single magnetic arcade often oscillate jointly (Schrijver et al. 2002; Verwichte et al. 2009). Jain et al. (2015) have reported that small phase shifts exist between such co-oscillating loops and suggest that such shifts could be caused by a moving driver or by the excitation of fast MHD waves that propagate across field lines from one loop to the other.

More recently, a distinct type of oscillation has been reported that is not clearly connected to any impulsive driver (Wang et al. 2012; Anfinogentov et al. 2013; Nisticò et al. 2013). These are low-amplitude oscillations and do not appear to exhibit a temporal decay. As such, some have called these oscillations "decayless." Anfinogentov et al. (2015) conducted a statistical analysis of 21 nonflaring active regions in the 171 Å bandpass of *SDO*/AIA in order to estimate the regularity of this phenomenon. The average

amplitude in the loop displacement is estimated to be 0.17 Mm, with periods ranging from 1.5 to 10 minutes. The nature of the driver of these oscillations remains unknown and various models have been suggested. Noting that these low-amplitude oscillations have poor phase coherence over long durations, Hindman & Jain (2014) considered a stochastically driven model of a 2D waveguide representing the entire coronal arcade. The decayless oscillations were excited by a distributed and stochastic source and appeared as a series of interference patterns formed by a multitude of MHD waves traveling through the waveguide. Nakariakov et al. (2016) have suggested that the decayless oscillations suffer the same decay mechanism as the flare-induced waves but supergranulation acts as a stochastic source that replenishes the lost energy.

In this paper, we present a new analysis method that uses autocorrelations of the traditional time–distance images to extract properties of the wave-field within the coronal arcade. This method has the salutary feature that it can be successfully applied to loops and arcades for which the traditional time–distance method would fail because of poor image contrast. We first validate this new method before illustrating these advantages. To do this, we measure the period of coronal loop oscillations using both our new procedure and the traditional time–distance method. We then compare the parameters measured with the two methods. Finally, we demonstrate the utility of the autocorrelation method in the detection of an additional periodicity in the form of low-amplitude oscillations that exist both long before and after the flares.

The paper is organized as follows. In Section 2, we describe the observational data and the chronological events that triggered the coronal loop oscillations. In Section 3, we present the image processing used to generate standard time–distance images of the oscillations. Subsequently, we present the results of a traditional fitting of the oscillations of the loops. In Section 4, we describe our new autocorrelation procedure, compare its results to the traditional method, and present an application of our new procedure to data for which the traditional fitting method would fail. Finally, in Section 5, we discuss the implications of our findings.

2. Observational Data

We study coronal loop oscillations on the southeastern limb using EUV images obtained by AIA/SDO with unprecedented spatial (1 pixel $\approx 0.6''$) and temporal (12 s cadence) resolutions on 2014 January 27. The arcade of interest belonged to a multipolar active region (AR) NOAA AR11967, which was behind the limb at the time of flare activity, and emerged a day later exhibiting a sunspot. The flaring activity is believed to have originated near the old active region AR11944 (S09, $L = 101$; see http://www.aurora-service.eu). While the flare is visible in all six EUV wavelengths, the arcade was predominantly visible in the 171, 193, and 211 Å channels and appeared as a bundle of illuminated arched threads, we refer to as loops. The data set was chosen due to the off-limb nature of the arcade, where the loops have a higher visibility contrast against the darkness of the background. For the entirety of our study, we examined 12 hr (3600 time frames) of EUV imagery, starting from 2014 January 26 20:00 UT and ending on 2014 January 27 08:00 UT.

Figure 1 displays an EUV snapshot of the coronal arcade above NOAA AR11967 observed through AIA 171 Å. Our analyses show that the loops embedded in the arcade were oscillating and overlapping with localized variations in amplitude before, during, and after the time of two consecutive

M1 class flares, which were near the southeastern limb and were recorded in X-rays by the GOES instruments. We investigate, in detail, the oscillations as they are manifested along the two slits indicated in the right panel of Figure 1.

Figure 2 shows the recorded X-ray flux by GOES in 4 and 8 Å. The first flare, located at latitude 16° south and longitude 88° east, was an M1.0 class flare, with a start time at 01:05 UT, a peak at 01:22 UT, and an end time at approximately 01:39 UT. After this an M1.1 class flare, at latitude 13° south and longitude 88° east, initiated at 02:02 UT, peaked at 02:11 UT, and ended at about 02:18 UT. Just before the first flare, a small wavefront was also seen propagating away from the limb and throughout the arcade. Initially, the wavefront appeared near the limb around 00:40 UT, and became evident at 01:00 when it started moving. The initial motion of the wavefront from the flare site was visible in the AIA movies in all six EUV wavelengths. The life-time of the wavefront, as seen in the 171 Å bandpass movie, is also marked in Figure 2 with a double-headed arrow. A summary of the major events are shown in Table 1. Additionally, coinciding with the time of both flares, STEREO-B/SWAVES recorded two Type III radio bursts.

After its initial stage of propagation, the wavefront was obscured by a bundle of several loops in the line of sight and so it was not possible to track it further. By carefully inspecting difference images, as shown in Figure 3, we measure the distance the wavefront traveled from the limb at three different times (see the middle panel). We estimate the wavefront to have an initial projected propagation speed of about 40 km s^{-1} from the slope of the line shown in the right panel.

3. Traditional Time–Distance Analysis

From the sequence of EUV images, it appears that the wavefront propagated away from the limb followed by the first M-class flare. The coronal loops above this AR were then seen oscillating during which a second flare occurred that did not excite further loop oscillations. To date, coronal loop oscillations have been analyzed by time-series fitting techniques (e.g., Verwichte et al. 2009; Jain et al. 2015; Weberg et al. 2018). We first carry out a similar procedure to extract the oscillatory parameters in the AIA 171 and 193 Å channels along an approximately 130 Mm long slit, indicated by Slit 1 in Figure 1, and also shown by the white line in Figure 4 (left panel). The slit was placed perpendicular to the axis of the arcade and the time–distance images were created by temporally stacking the intensity along the slit at the AIA cadence. In order to remove small spatial-scale noise, we increase the signal-to-noise by smoothing the intensity over a width of about 2 Mm on either slide of the slit. The resultant intensity variations are shown in the right panels of Figure 4, where the origin of the time–distance image corresponds to the bottom right point of Slit 1. The upper and lower panels correspond to the 171 Å and the 193 Å bandpasses, respectively. It is important to highlight that the phase relations of oscillations observed within slits may be dependent on the orientation. Studies of 3D coronal loop reconstructions have demonstrated that, due to projection effects, the choice of a slit is not trivial and cannot be guaranteed to be along the projected displacement of a bundle of loops (e.g., Verwichte et al. 2009).

Furthermore, to accurately extract the oscillatory properties with detail, the waveforms must be seen clearly with well-defined amplitude boundaries. In order to do this, the time–distance images were further enhanced by convolving the
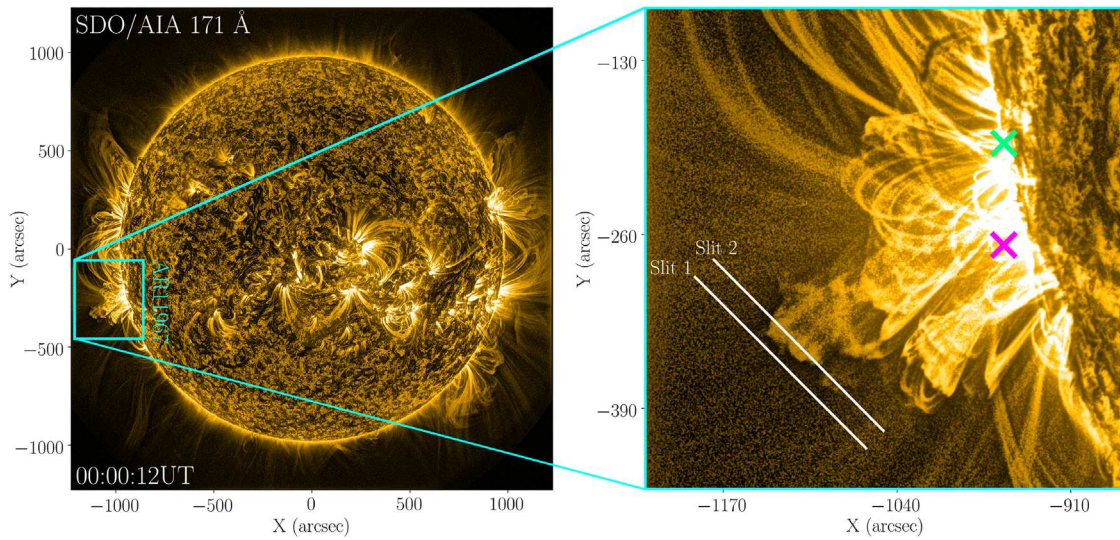
Figure 1. EUV image at the beginning of the data set on 2014 January 27 00:00:12UT observed with *SDO*/AIA 171 Å. Left panel: full-disk image indicating the active region of interest. Right panel: zoomed-in view of the area contained in the box. The solid white lines correspond to a ∼130 Mm slit placed transverse to the apparent arcade. The magenta and green crosses correspond to the approximate positions of the flaring activity. The analyses of the loop oscillations are performed separately on each of these two numbered slits. Note that this image has been enhanced with the multiscale Gaussian normalization (Morgan & Druckmuller 2014).
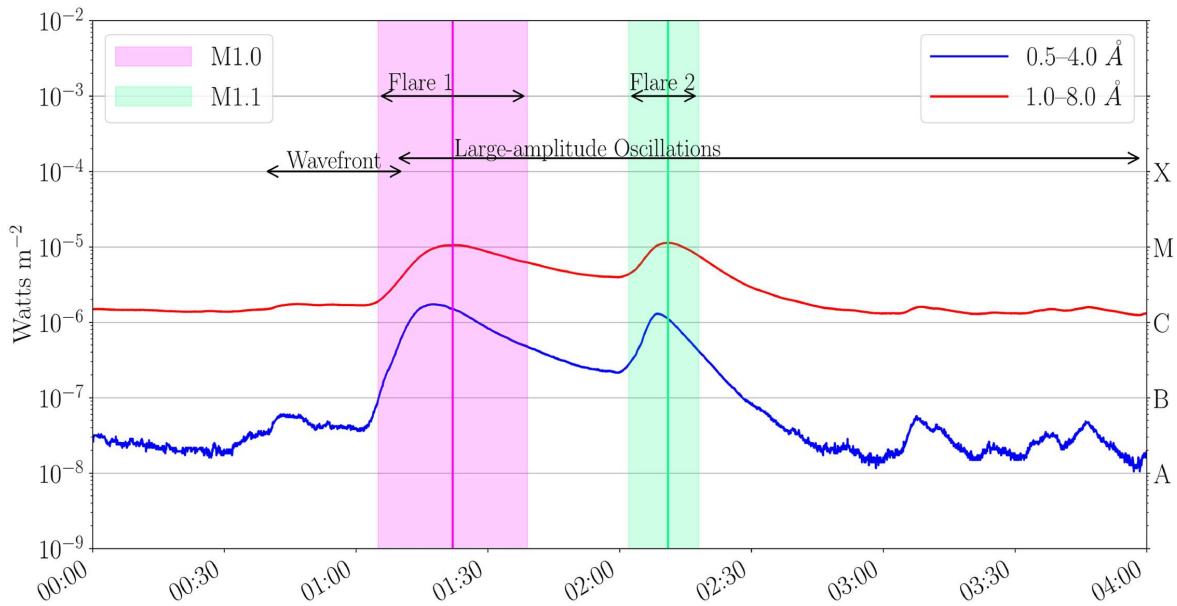

Figure 2. Energy flux of the two M-class flares near NOAA AR11967 as detected by the *GOES* instrument. The magenta and green lines show the peak times of the first and second flares, respectively. The shaded areas correspond to the onset and final flare times. The duration of the wavefront and the coronal loop oscillations are also indicated by arrows.

Table 1
A Chronological Summary of the Impulsive Events that Occurred in AR11967 as Observed by AIA

Event	Duration (UT)	Comments
Wavefront	00:55–01:05	Visible in all EUV channels.
1st Flare	01:05–01:39	M1.0 class.
2nd Flare	02:02–02:18	M1.1 class. No wavefront observed.
Large-amplitude oscillations	01:10–04:00	Predominant in 171, 193 and 211 Å.

image with a weighted 3 × 3 kernel of the form:

$$\begin{pmatrix} 1 & 2 & 1 \\ 0 & 0 & 0 \\ -1 & -2 & -1 \end{pmatrix}. \tag{1}$$

This convolution performs a triangular temporal smoothing to the time–distance images and takes a numerical derivative with respect to the spatial position along the slit. As a result, the contrast is enhanced at the loop edges. Figure 5 presents the processed time–distance image for the 193 Å bandpass, highlighting a variety of oscillating loops. These oscillations
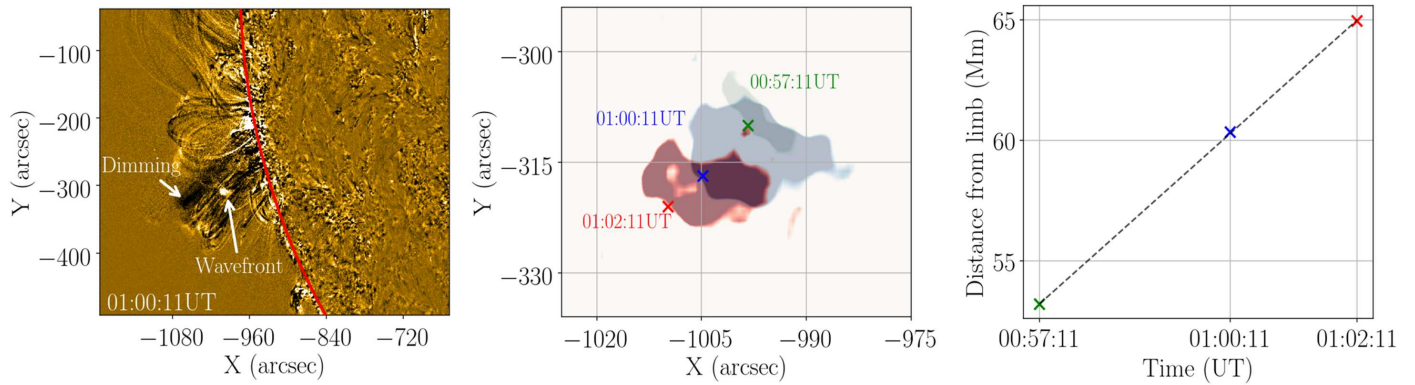
Figure 3. Left panel: base difference image revealing the wavefront before the onset of the first flare. The solar limb is indicated by the solid red line. Middle panel: composite snapshots of the wavefront at three different times. Right panel: projected initial distance of the wavefront from the solar limb as a function of time.
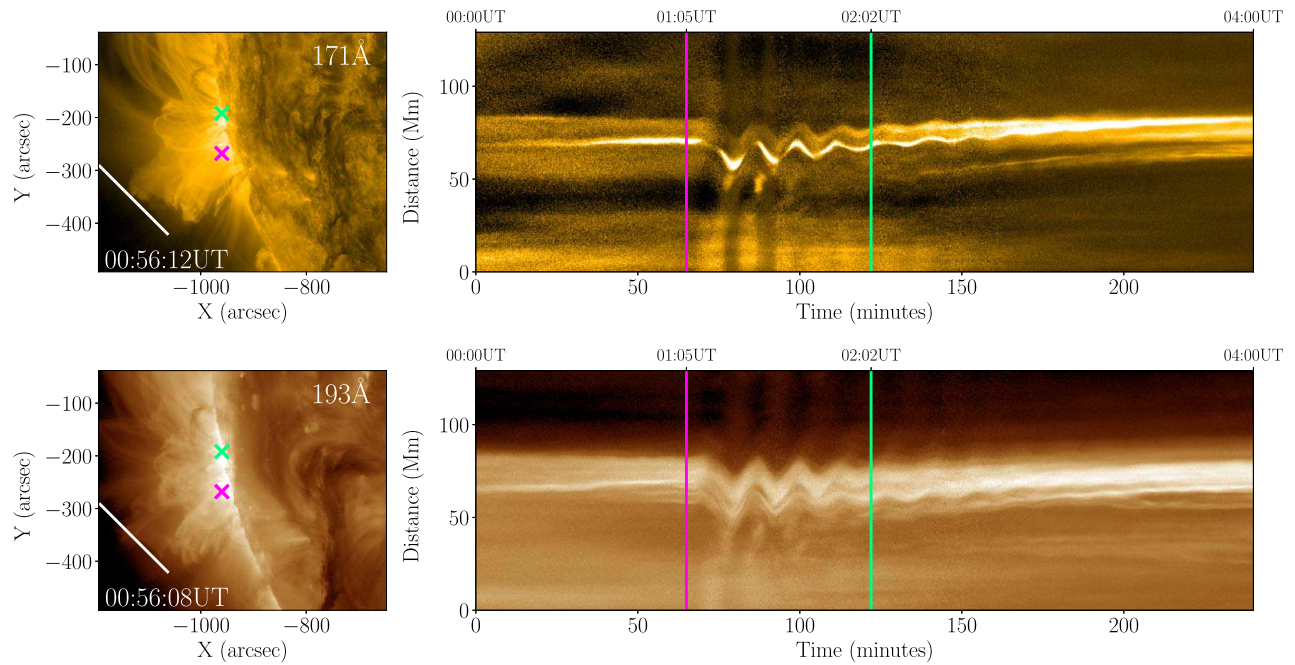

Figure 4. Coronal arcades and oscillations. Left panels: EUV snapshots in the 171 Å (top) and 193 Å (bottom) channels, with Slit 1 indicated by the white line. The magenta and green lines indicate the onset times of the flares. Right panel: the corresponding intensity variations along Slit 1 in the aforementioned channels as a function of time.
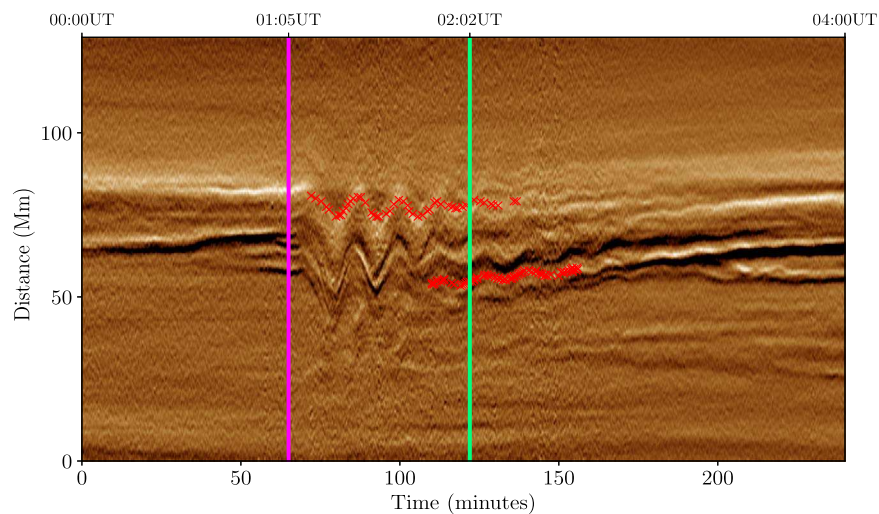

Figure 5. Convolved time–distance image for the intensity variations as seen in the 193 Å bandpass, shown in Figure 4. The red crosses overplotted on top of the time–distance image are from the resultant time series fits.
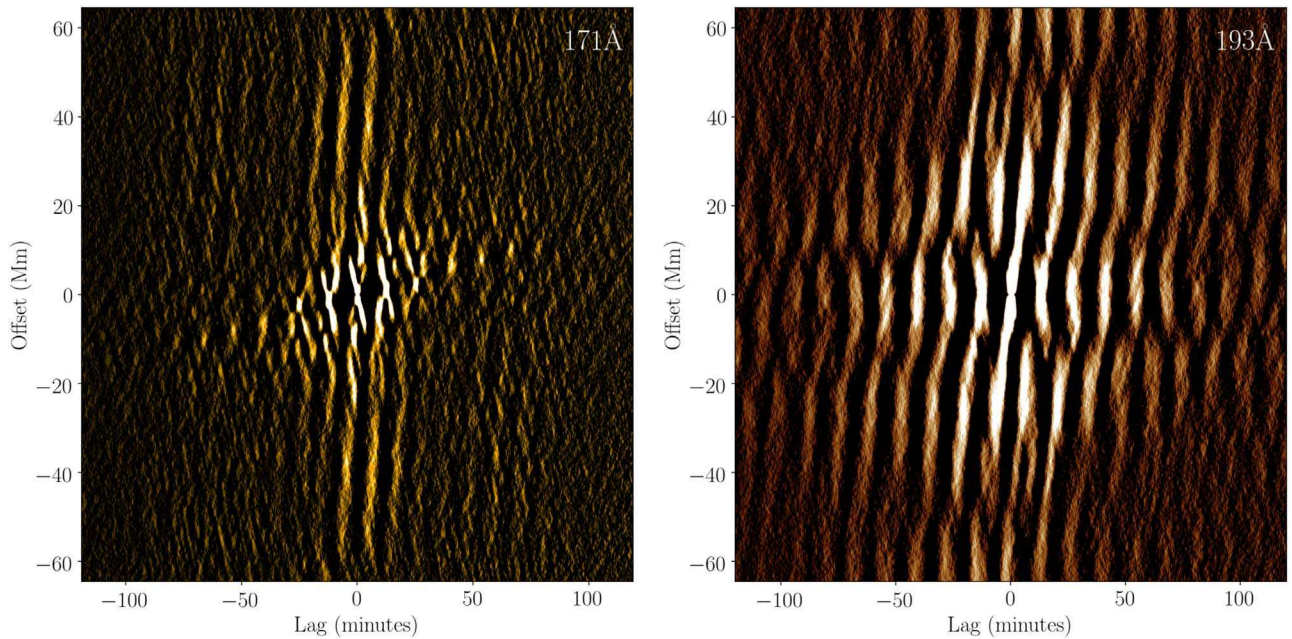
Figure 6. Autocorrelations of the time–distance images generated as a function of spatial offset (megameters) and time lag (minutes) for Slit 1 in the 171 Å (left) and 193 Å (right) bandpass.

Table 2
Fitted Parameters from Time–Distance Fitting Methods

Wavelength (Å)	Amplitude (Mm)	Period (minutes)	Damping Time (minutes)	Phase (°)
171 (large-amplitude)	(5.20 ± 0.75)	(13.00 ± 0.06)	(34.43 ± 11.12)	(65.99 ± 3.73)
193 (large-amplitude)	(3.30 ± 0.76)	(13.02 ± 0.12)	(48.30 ± 2.70)	(-98.98 ± 6.57)
193 (small-amplitude)	(0.68 ± 0.12)	(14.03 ± 0.21)	...	(20.38 ± 10.31)

are also clearly visible in 171 and 211 Å but less so in the 94 and 131 Å channels.

The dominant loop featured in Figure 5 undergoes a large-amplitude decaying oscillation. Interestingly, in addition to this, there were weaker small-amplitude oscillations that commenced near the onset of the second flare. These weaker oscillations appear near the bottom of the bundle of main loops. By fitting a Gaussian locally to the intensity of each pixel, we find the position of maximum brightness as a function of time and generate the time series. We fit the time series with appropriate sinusoidal functions of the form $\mathcal{A}\exp(-t/\tau)\cos(2\pi t/T + \phi)$, where $\mathcal{A}$ is an amplitude, T is a period, τ is a damping time, and ϕ is a wave phase. The resultant fits are shown in Figure 5 as a sequences of red crosses and the fitting parameters are summarized in Table 2. To stabilize the fit of the small-amplitude oscillations, the decay rate τ^{-1} was fixed to zero.

4. Autocorrelation Analysis

The intensity variations within traditional time–distance images contain an abundance of information about bright loops. However, the standard time–distance analysis cannot capture these oscillations when the loops are not well-defined. For example, oscillations in the presence of complex, overlapping, and faint loops will result in inaccuracies of the time-series fitting parameters. In such a circumstance the loops cannot be fitted with fidelity and the method fails. In this section, we demonstrate the use of a new method that exploits

autocorrelations of the raw time–distance images. We generate a 2D normalized autocorrelation function, which describes the degree of similarity of the image with itself as it is shifted both temporally and spatially along the slit. As we will see, this procedure reveals the periodicities that remain hidden in the traditional time–distance analysis.

Many of the sharpest features in the time–distance images (as shown in Figure 4) are fairly stationary as a function of time. Therefore, the application of a temporal high-pass filter will generate smooth images by removing a background. To accomplish this and to remove spurious signals from the steady features in each pixel, we compute a high-pass filtered image $\widetilde{I}(t, x)$ by subtracting a background intensity image $I_b(t, x)$ from the original time–distance images $I(t, x)$,

$$\widetilde{I}(t, x) = I(t, x) - I_b(t, x), \qquad (2)$$

where t is the temporal coordinate and x is the spatial position along the slit. The background intensity I_b is computed by convolving the original time–distance image with a Gaussian kernel of standard deviation $\sigma = 10$ frames along the temporal coordinates. Thus, the small-scale fluctuations in the intensities are smoothed out within every two-minute time interval. By subtracting this background from the original intensity, the resultant linearly filtered high-pass image mitigates low-frequency variations in order to sharpen the oscillatory features inherent within the original time-series.
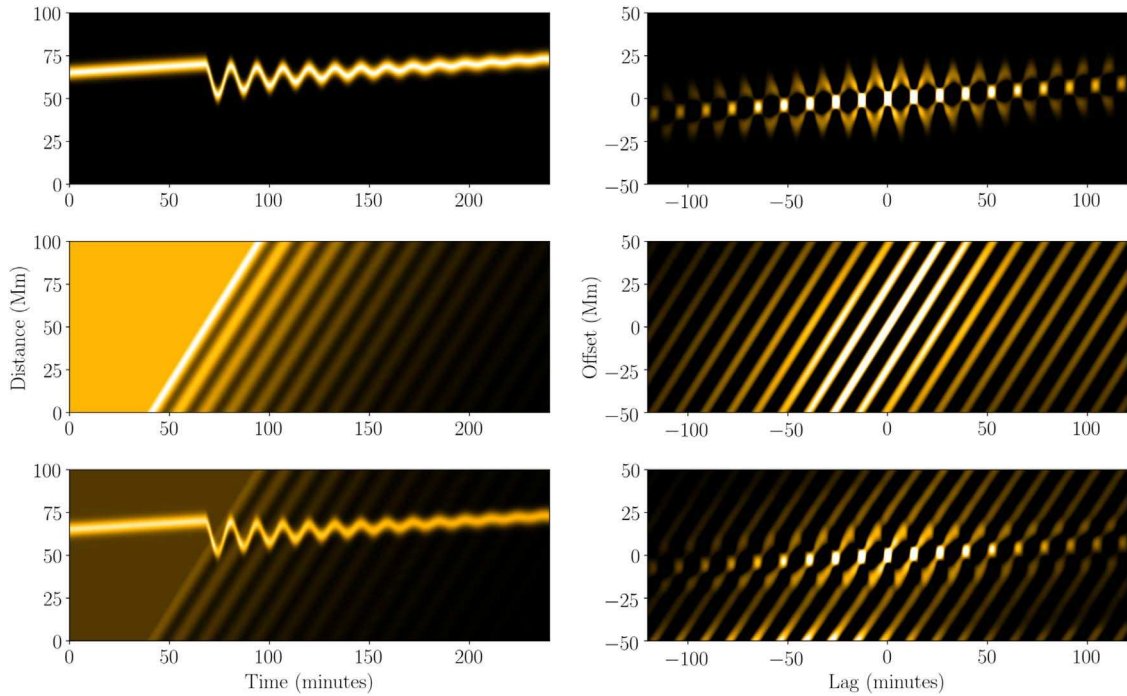
Figure 7. Artificial time–distance images (left) and their autocorrelations (right). Top panel: bright loop that suddenly begins oscillating, undergoes temporal decay, and slowly drifts along the slit. The autocorrelation of the bright loop with itself reveals a set of Xs whose centers are sloped according to the linear drift of the loop along the slit. Middle panel: background of faint loops that begin oscillating at different times thus introducing a phase shift that varies along the slit. The autocorrelation of the bundle of faint loops reveals tilted streaks whose slopes are fixed by the spatially varying phase between the different slit positions. Bottom panel: bright and faint loop background superimposed. The prominence of the Xs depends on the relative brightness of the bright loop to the bundle of faint loops.

The autocorrelation is defined in the standard manner as a function of time lag Δt and spatial offset Δx,

$$c(\Delta t, \Delta x) = \iint \tilde{I}(t, x)\tilde{I}(t + \Delta t, x + \Delta x)\, dt dx. \qquad (3)$$

The integrals are approximated with discrete sums. We first zero-pad the time-domain signals and then generate a normalized autocorrelation $C(\Delta t, \Delta x) \equiv c(\Delta t, \Delta x)/c(0, 0)$. The periodic structures within the image are therefore revealed by a strong autocorrelation at the corresponding spatial offsets and time lags.

Figure 6 displays the autocorrelation as a function of spatial offset (measured in megameters) and time lag (measured in minutes) for the 171 Å (left) and 193 Å (right) wavelength bandpass. As expected, the maximum correlation occurs at zero time lag. The near-vertical streaks have a slope due to the phase shift that exists among the multitude of oscillating loops sampled along the slit. Very noticeable X-like features are aligned in a sequence across time-lag with a different shallower slope. These Xs are most prominent in the 171 Å channel and nearly invisible in the 193 Å bandpass.

In order to understand the origin of the various slopes and features evinced by these autocorrelations, we created a synthetic data set that consists of a bright oscillating loop embedded in a background of fainter dispersed loops that are also oscillating. The upper-left panel of Figure 7 shows the time–distance image of the bright loop in isolation. This bright loop starts oscillating, decays rapidly, and slowly drifts upward along the slit as time passes. The upper right panel reveals the 2D autocorrelation of this bright loop. We immediately see that the X-like structures that we observed in the autocorrelation of the coronal imagery is due to a bright oscillating loop correlating with itself. Furthermore, the slope in the line

passing through the centers of the sequence of Xs is caused by the temporal drift of the loop along the slit, possibly due to a moving driver or the wavefront.

The middle left panel of Figure 7 shows the background of dispersed faint loops and the middle-right panel shows their autocorrelation. These figures make it clear that the tilted vertical streaks in Figure 6 are due to the bundle of faint loops inherent in the background of the image. The slope of the streaks arises from a phase shift between these loops in the bundle where the phase changes slowly along the slit. Finally, in the lower left panel of Figure 7 we show the superposition of the time–distance image for the bright loop and the bundle of faint loops. The corresponding autocorrelation in the lower right panel demonstrates that the prominence of the X-like features depends on the relative brightness contrast between the bright loop and the faint loop background and the relative phase shift. Note that in Figure 4 there is a clear bright loop in the 171 Å channel (upper right panel) with a well-defined amplitude and period; however, due to the relative contrast and the presence of a background of multiple faint loops, the same bright loop viewed in the 193 Å bandpass appears only marginally brighter (lower right panel). For this reason, the sequence of Xs is not so obvious in the autocorrelation of the time–distance image of the 193 Å bandpass.

4.1. Comparison of the Two Methods

The autocorrelation contains a plethora of information about the oscillations, e.g., the phase coherence of the primary oscillations over multiple periods, whether the oscillation periods drift with time, phase relations between different oscillating structures, etc. However, at the moment, we will extract only the period of the dominant periodicity so that we
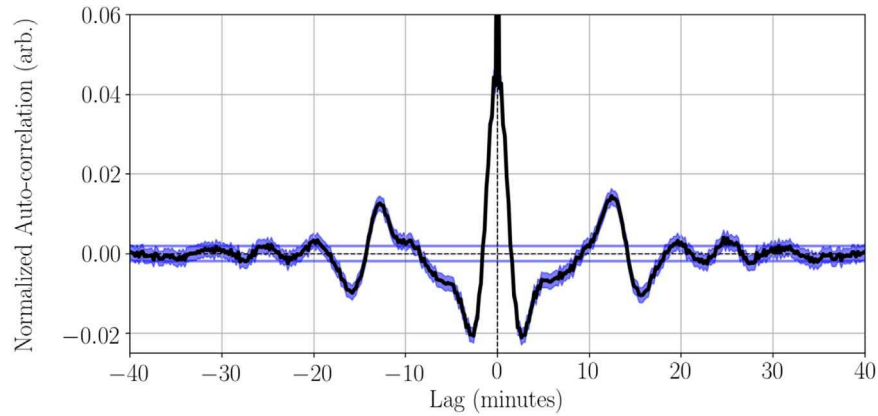
Figure 8. Normalized autocorrelation function averaged over a narrow range of spatial offsets (between −3.5 and 3.5 Mm) and plotted vs. time lag. Each X-like feature in Figure 6 (left panel) produces a peak of positive correlation. The time lag of peak correlation for the first set of side lobes (to the right and left of the central correlation) corresponds to the dominant period of oscillation. The 5% confidence intervals are shown with the solid blue lines.

can verify that our autocorrelation procedure and the traditional time series fitting method generate consistent results.

The dominant period of oscillation can be obtained by measuring the location of the peaks (centers of the Xs) in the autocorrelation immediately to the left and right of the central peak at a time lag of zero (see Figure 6). To illustrate these peaks, we average the autocorrelation over a band of spatial offsets, $\Delta x \in [-3.5 \text{ Mm}, \ 3.5 \text{ Mm}]$. This average is performed separately at each time lag Δt and the result is shown in Figure 8. The central peak arises from the correlation of the signal with itself at the same time. The peaks to the right and left come from correlating the current period with either the previous or the following period in the oscillation. Thus, the autocorrelation peaks at a time lag that corresponds to the wave period.

By fitting a Gaussian to the time lag of maximum correlation for the first side peaks we deduce that the dominant oscillation within Slit 1 has a period of (12.31 ± 0.02) minutes, a number consistent with the 13 minute period measured using the traditional method. If the oscillations were long-lived with steady periods, we would expect to see peaks at each multiple of the period as well and the amplitude of each peak would attenuate only slowly with time lag. That is clearly not the case here. We do see enhanced correlation at 25–26 minutes but the autocorrelation value drops rapidly from peak to peak, as one would expect for a rapidly decaying oscillation for which the higher multiples have fewer periods over which to correlate.

4.2. Application of the Autocorrelation Method to Complex Bundles of Loops

One of the advantages of the autocorrelation procedure is its ability to analyze loop systems for which the standard fitting method would fail. In particular, the autocorrelation procedure presented here can analyze bundles of loops that are poorly differentiated and criss-cross each other. As an illustration, we will analyze the intensity variations on Slit 2, which samples the arcade closer to the limb. On this slit many loops coexist in a complicated overlapping pattern. Furthermore, we will analyze oscillations in periods that lie well before the initiating flares and well after. The goal is to seek low-amplitude "decayless" oscillations that would be too weak to otherwise fit.

In Figure 9, we show the intensity variations as they appeared on Slit 2 in AIA 171 Å (see Figure 1 for the location

of Slit 2). The upper panel shows the time–distance diagram for a pre-flare phase that spans the 4 hr immediately prior to the analyses presented previously in this paper (20:00–24:00 on 2014 January 26). The middle panel displays the flaring phase (0:00–04:00 on 2014 January 27), which identically matches the 4 hr period that was previously examined in detail for Slit 1. The bottom panel presents the post-flare phase, which is the subsequent 4 hr period (04:00–08:00 on 2014 January 27). Recall that the duration of flare activity reported by *GOES* was from 01:05 to 01:39 UT on 2014 January 27. Note that weak oscillation signatures (due to "decayless oscillations") do appear in the pre- and post-flare phases. However, the loop structure is so complicated and the oscillations so weak that it is not possible to extract the oscillation parameters by the standard fitting procedure as outlined earlier in Section 3.

Figure 10 shows the autocorrelation functions derived from the three time durations indicated in Figure 9. The top, middle, and bottom panels correspond to the pre-flare phase, flaring phase, and post-flare phase, respectively. The oscillations illustrated in the middle panel correspond to the same flare-induced oscillations discussed previously, but viewed at a position closer to the limb. There is a primary period and multiples of that period. All of the loops along the slit oscillate in concert, but do so with a phase shift that changes roughly linearly along the slit (as discussed in Section 4). Furthermore, the lack of clear Xs indicates that the entire bundle of loops contributes without a single dominant loop.

In the pre- and post-flare duration (top and bottom panel of Figure 10), we see that the correlation has little signals for spatial offsets of much more than 5 Mm. There is a slight slope to the correlation that corresponds to a drift of the loop system along the slit as time passes. However, the concentration of signal near a spatial offset of zero indicates that loops do not correlate well with each other. We do, however, find that the temporal correlation possesses structure. For the pre-flare phase we see a central lobe at zero time lag and a single obvious side-lobe to each side of the central lobe. For the post-flare phase, there are additional side lobes located at multiples of the time lag of the primary side lobes. The simplest interpretation of these observations is that there is a primary frequency of oscillation at which each loop oscillates. However, different loops along the slit lack coordination and oscillate at essentially random phases, suggesting that the temporal phase coherence of these small-amplitude oscillations are poor. In the pre-flare
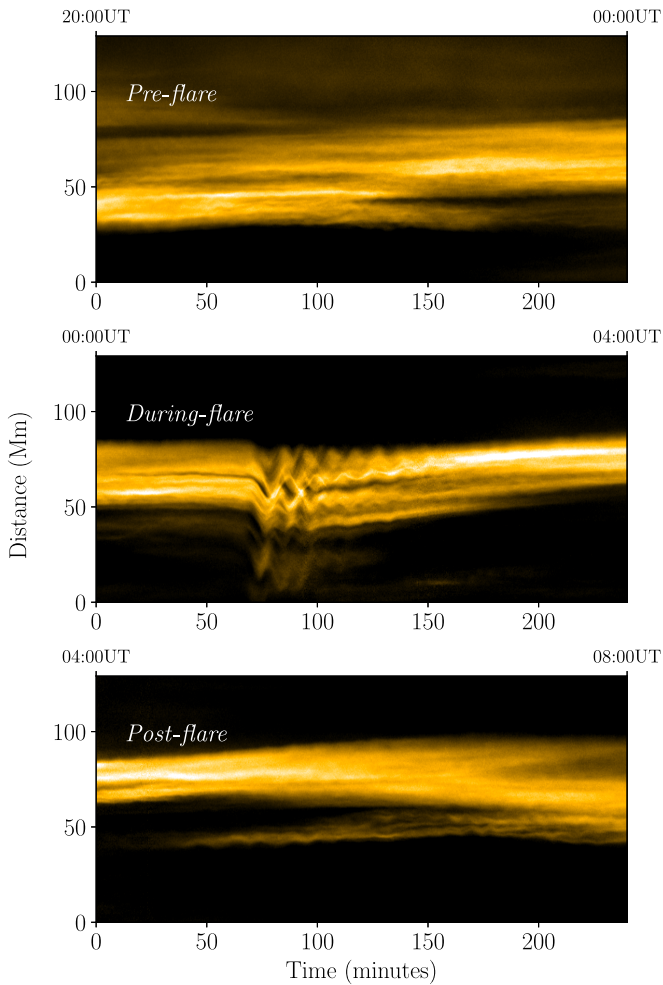
Figure 9. Intensity variations in 171 Å bandpass as observed on Slit 2 closer to the limb. Top panel: the time–distance diagram for a pre-flare phase (20:00–24:00 on 2014 January 26). Middle panel: intensity variations during a phase coeval with the flares (0:00–04:00 on 2014 January 27). This temporal window is identical to the one used to analyze the oscillations on Slit 1 (see Figure 4). Bottom panel: the time–distance diagram for a post-flare phase (04:00–08:00 on 2014 January 27). Small-amplitude "decayless" oscillations are present before and after the flares, but their displacements cannot be fitted due to the complex structure of the loop bundle. During the flaring phase, large-amplitude flare-induced oscillations exist, but once again the overlapping loops make the fitting of those loops problematic.

Figure 10. 2D autocorrelations of time–distance diagrams appearing in Figure 9 obtained for Slit 2. Top panel: the autocorrelation for the pre-flare phase. Middle panel: the autocorrelation for the flaring phase (from 00:00 to 04:00 UT on 2014 January 27). Bottom panel: autocorrelation of the post-flare phase (from 04:00 to 08:00 UT on 2014 January 27). All are for the 171 Å bandpass. The pre-flare and post-flare images reveal the existence of decayless oscillations whose lack of long spatial correlations indicate that different loops oscillate incoherently. Furthermore, the presence of only one or two side lobes on each side of the central correlation indicate poor phase coherence with time.

phase the amplitude is sufficiently low that only correlations with the immediately preceding or following phase is possible before noise (or another periodicity) dominates. In the post-flare phase the amplitude is larger, and we can see correlations arising from shifts of two or more wave periods.

The exact periods of oscillation can be extracted from line plots of the autocorrelation at zero spatial offset. Averaging over a width containing the Xs, one obtains the correlations shown in Figure 11. The dominant period of oscillation in the flaring phase is (10.05 ± 0.01) minutes and (9.81 ± 0.08) minutes in the post-flare phase. The dominant period is slightly shorter in the pre-flare phase at (9.13 ± 0.10) minutes.

5. Discussion

5.1. Oscillations during the Flares

The primary period of oscillation of the flare-induced waves is clearly a function of the position of the slit. The oscillations
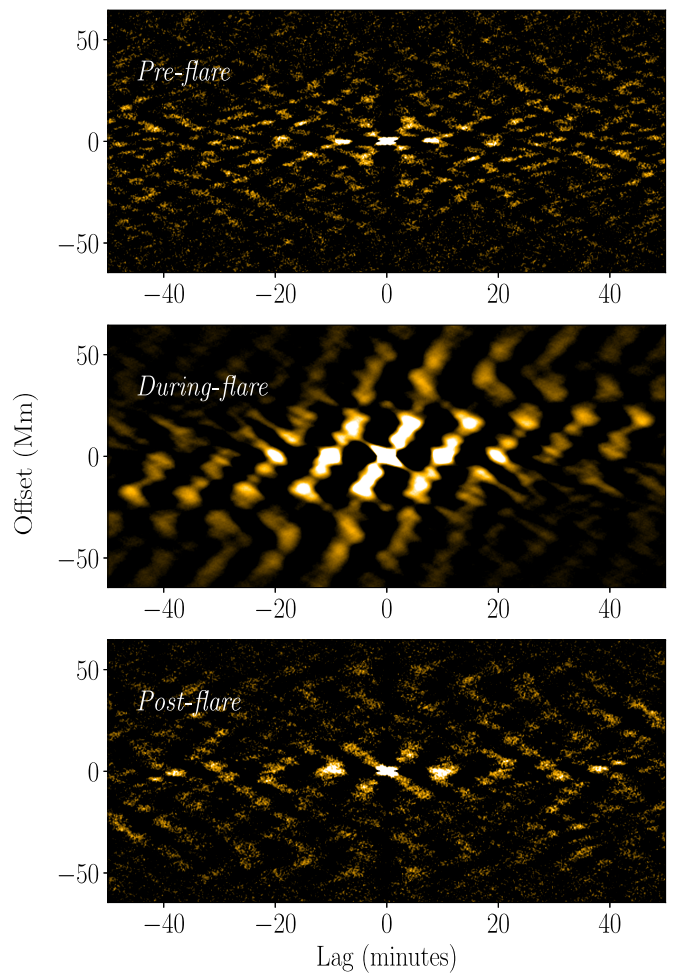
observed on Slit 1, the slit furthest from the limb, possessed a dominant period of 12.31 minutes, while the slit closer to limb, Slit 2, had a shorter period, 10.05 minutes. Without performing similar analyses along a plethora of slits, we cannot ascertain whether the dominant period is a smooth function of height above the limb.

Hindman & Jain (2015) have argued that the bundles of magnetic loops in an arcade oscillate together and that the true cavity is multidimensional as opposed to an individual loop. Figures 4 and 5 clearly suggest this. Nearby loops are likely to have similar lengths, magnetic field strengths, and densities and so we expect the entire arcade to oscillate with similar periods in response to the driver. Loops at different positions along the slit oscillate with phase shifts relative to each other and those phases change roughly linearly along the slit. If the waves propagate both along the field and transverse to the field, then we must entertain the possibility that magnetic pressure also plays a role, even if magnetic tension is the main restoring force. The motions studied here, are clearly transverse to the magnetic field lines and the phase shift appears to be traveling
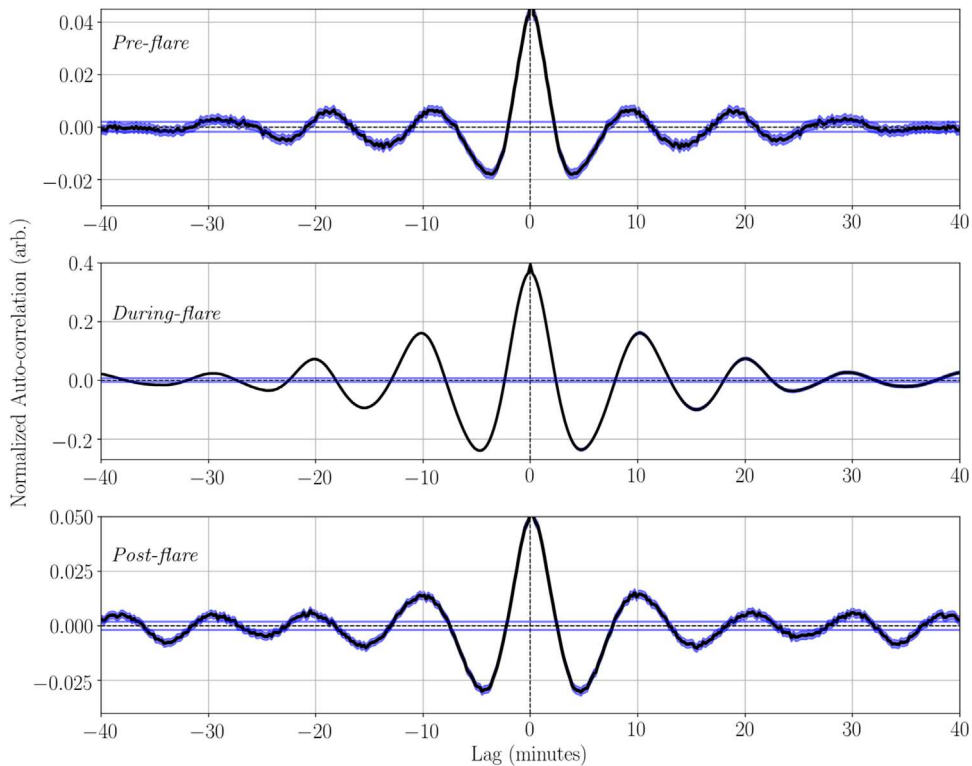
Figure 11. Normalized autocorrelation function generated in the same manner as Figure 7. The autocorrelations used to generate each panel are those shown in Figure 10. Top panel: autocorrelation for the pre-flare phase. Middle panel: autocorrelation for the flaring phase. Bottom panel: autocorrelation for the post-flare duration.

across the magnetic field lines. This suggests that there is a compression of magnetic field lines, perhaps, indicating the presence of fast MHD waves.

To test this idea further, we measure the speed of phase propagation along the slit directly from the slope of the near-vertical streaks in the autocorrelation diagrams. Doing so produces a phase speed of $140\,\mathrm{km\,s^{-1}}$ for the 171 Å bandpass and about $62\,\mathrm{km\,s^{-1}}$ for the 193 Å bandpass. Both slits generate similar phase speed values. These speeds are sufficiently low compared to the local Alfvén speed that if the phase shift was caused by cross-field propagation the wave vector would need to be strongly radial, with only a small component aligned with the slits.

A more likely interpretation for such a phase shift is a moving driver. Recall that the initial propagation speed of the wavefront was $40\,\mathrm{km\,s^{-1}}$ as projected on the plane of the sky. The similarity of this speed with the speed of phase propagation may be coincidental but it may also suggest that the wavefront acted as a moving wave-excitation source. This conclusion is further supported by the observation that the large-amplitude flare-induced oscillations appear to have been excited slightly before the occurrence of the peak of the X-ray flux from the first flare was recorded by the *GOES* observatories.

5.2. Oscillations before and after the Flares

Along Slit 2, we see oscillations before, during, and after flaring activity. Prior to the flares the dominant period appears to be 9.13 minutes and each strand of the bundle of loops appears to oscillate rather incoherently with more distant strands. Well after the flares, the primary period appears to be 9.81 minutes and, once again, the individual loops that are

well-separated oscillate somewhat incoherently. The correlation length in both cases is roughly 5 Mm. We reiterate and emphasize that the low-amplitude oscillations presented here would be laborious to fit with the traditional time–distance fitting method with fidelity due to the complexity of overlapping loops. The autocorrelation method presented is a promising tool for analyzing small-amplitude waves in coronal arcades at all times. Detailed studies of the prevalence of such complex small-amplitude oscillations can now be conducted with the key advantages of being simpler to implement and being able to form parts of automated search tools.

It is possible that the difference in dominant period between the pre-flare and post-flare phases (9.13 minutes and 9.81 minutes, respectively) indicates a change in the arcade's resonant structure. The heating induced by the flares may have initiated a change in Alfvén speed along the loops under analysis. We note, however, that a similar change in apparent frequency may arise from a change in the distribution of waves with different cross-field wavenumber. Hindman & Jain (2015, 2018) have demonstrated that coronal arcades can act as waveguides, with resonances only in the radial direction (radial to the limb) and in the direction parallel to the field lines. The direction along the axis of the arcade (in this case parallel to the slit), may be unquantized. Each axial wavenumber has a different frequency and when energy is redistributed among this continuum of wavenumbers, the distribution of energy among modes with different periods is changed. One piece of evidence that supports this latter scenario is that the large-amplitude oscillations that were initiated during the flaring activity also have a dominant period of 10 minutes along Slit 2. It could very well be that the post-flare phase is dominated by waves initiated during the flare that

have decayed in amplitude. Thus, the intensity variations in the post-flare phase may be a superposition of oscillations of periodicities of 9 and 10 minutes.

ORCID iDs

Farhad Allian ● https://orcid.org/0000-0002-4569-0370
Rekha Jain ● https://orcid.org/0000-0002-0080-5445
B. W. Hindman ● https://orcid.org/0000-0001-7612-6628

References

Anfinogentov, S., Nakariakov, V. M., & Nisticò, G. 2015, A&A, 583, A136
Anfinogentov, S., Nisticò, G., & Nakariakov, V. M. 2013, A&A, 560, A107
Aschwanden, M. J., De Pontieu, L., Schrijver, C. J., & Title, A. M. 2002, SoPh, 206, 99
Aschwanden, M. J., Fletcher, L., Schrijver, C. J., & Alexander, D. 1999, ApJ, 520, 880
Brady, C. S., & Arber, T. D. 2005, A&A, 438, 733
Edwin, P., & Roberts, B. 1983, SoPh, 88, 179
Goossens, M., Andries, J., & Aschwanden, M. J. 2002, A&A, 394, L39
Hindman, B. W., & Jain, R. 2014, ApJ, 784, 103
Hindman, B. W., & Jain, R. 2015, ApJ, 814, 105
Hindman, B. W., & Jain, R. 2018, ApJ, 858, 6
Jain, R., Maurya, A. R., & Hindman, B. W. 2015, ApJL, 804, L19
Lemen, J. R., Title, A. M., Akin, D. J., et al. 2012, SoPh, 275, 17
Li, H., Liu, Y., & Vai Tam, K. 2017, ApJ, 842, 99
Morgan, H., & Druckmuller, M. 2014, SoPh, 289, 2945
Nakariakov, V. M., Ofman, L., Deluca, E. E., Roberts, B., & Davila, J. M. 1999, Sci, 285, 862
Nakariakov, V. M., Pilipenko, V., Heilig, B., et al. 2016, SSRv, 200, 75
Nisticò, G., Nakariakov, V. M., & Verwichte, E. 2013, A&A, 552, A57
Roberts, B., Edwin, P., & Benz, A. 1984, ApJ, 279, 857
Ruderman, M. S., & Roberts, B. 2002, ApJ, 577, 475
Schrijver, C. J., Aschwanden, M. J., & Title, A. M. 2002, SoPh, 206, 69
Selwa, M., Murawski, K., Solanki, S. K., & Wang, T. J. 2007, A&A, 462, 1127
Smith, J. M., Roberts, B., & Oliver, R. 1997, A&A, 317, 752
SunPy Community, Mumford, S. J., Christe, S., et al. 2015, CS&D, 8, 014009
Verwichte, E., Aschwanden, M., Van Doorsselaere, T., & Nakariakov, V. 2009, ApJ, 698, 397
Verwichte, E., Foullon, C., & Nakariakov, V. M. 2006a, A&A, 446, 1139
Verwichte, E., Foullon, C., & Nakariakov, V. M. 2006b, A&A, 449, 769
Wang, T., Ofman, L., Davila, J. M., & Su, Y. 2012, ApJL, 751, L27
Weberg, M., Morton, R. J., & McLaughlin, J. A. 2018, ApJ, 852, 57